



HAL
open science

Recent advances toward mesoscopic quantum optomechanics

M Croquette, S Deleglise, T Kawasaki, K Komori, M Kuribayashi, A
Lartaux-Vollard, N Matsumoto, Y Michimura, M Andia, N Aritomi, et al.

► **To cite this version:**

M Croquette, S Deleglise, T Kawasaki, K Komori, M Kuribayashi, et al.. Recent advances toward mesoscopic quantum optomechanics. *AVS Quantum Science*, 2023, 5 (1), pp.014403. 10.1116/5.0128487 . hal-04079917

HAL Id: hal-04079917

<https://hal.science/hal-04079917v1>

Submitted on 7 Jan 2025

HAL is a multi-disciplinary open access archive for the deposit and dissemination of scientific research documents, whether they are published or not. The documents may come from teaching and research institutions in France or abroad, or from public or private research centers.

L'archive ouverte pluridisciplinaire **HAL**, est destinée au dépôt et à la diffusion de documents scientifiques de niveau recherche, publiés ou non, émanant des établissements d'enseignement et de recherche français ou étrangers, des laboratoires publics ou privés.



Distributed under a Creative Commons Attribution 4.0 International License

Recent advances toward mesoscopic quantum optomechanics

Cite as: AVS Quantum Sci. 5, 014403 (2023); <https://doi.org/10.1116/5.0128487>

Submitted: 28 September 2022 • Accepted: 04 January 2023 • Published Online: 03 February 2023

 M. Croquette,  S. Deléglise,  T. Kawasaki, et al.

COLLECTIONS

Paper published as part of the special topic on [Quantum Acoustics](#)



View Online



Export Citation

ARTICLES YOU MAY BE INTERESTED IN

[Distributed acoustic sensing recordings of low-frequency whale calls and ship noise offshore Central Oregon](#)


JASA Express Letters **3**, 026002 (2023); <https://doi.org/10.1121/10.0017104>

[Influence of nano-indentation depth on the elastic-plastic transformation of 6H-SiC simulated](#)
AIP Advances **13**, 025118 (2023); <https://doi.org/10.1063/5.0132934>


Chinese Abstracts

Chinese Journal of Chemical Physics **35**, i (2022); <https://doi.org/10.1063/1674-0068/35/06/cabs>





HIDEN
ANALYTICAL



40
YEARS
1982 - 2022


Instruments for Advanced Science

- Knowledge,
- Experience,
- Expertise

Click to view our product catalogue


Contact Hiden Analytical for further details:
www.HidenAnalytical.com
info@hideninc.com

Gas Analysis




- ▶ dynamic measurement of reaction gas streams
- ▶ catalysis and thermal analysis
- ▶ molecular beam studies
- ▶ dissolved species probes
- ▶ fermentation, environmental and ecological studies

Surface Science




- ▶ UHVTPD
- ▶ SIMS
- ▶ end point detection in ion beam etch
- ▶ elemental imaging - surface mapping

Plasma Diagnostics



- ▶ plasma source characterization
- ▶ etch and deposition process reaction kinetic studies
- ▶ analysis of neutral and radical species

Vacuum Analysis



- ▶ partial pressure measurement and control of process gases
- ▶ reactive sputter process control
- ▶ vacuum diagnostics
- ▶ vacuum coating process monitoring

Recent advances toward mesoscopic quantum optomechanics

Cite as: AVS Quantum Sci. 5, 014403 (2023); doi: 10.1116/5.0128487

Submitted: 28 September 2022 · Accepted: 4 January 2023 ·

Published Online: 3 February 2023



View Online



Export Citation



CrossMark

M. Croquette,¹ S. Deléglise,¹ T. Kawasaki,^{2,3} K. Komori,^{4,5} M. Kuribayashi,⁶ A. Lartaux-Vollard,⁷ N. Matsumoto,⁸ Y. Michimura,^{5,9} M. Andia,⁷ N. Aritomi,¹⁰ R. Braive,¹¹ T. Briant,¹ S. Briauudeau,¹² S. B. Cataño-Lopez,¹³ S. Chua,^{1,a)} J. Degallaix,¹⁴ M. Fujimoto,¹⁰ K. Gerashchenko,¹ F. Glotin,⁷ P. Gruning,⁷ K. Harada,⁶ A. Heidmann,¹ D. Hofman,¹⁴ P.-E. Jacquet,¹ T. Jacqmin,¹ O. Kozlova,¹² N. Leroy,⁷ V. Lorette,¹⁵ F. Loubar,¹² T. Martel,¹¹ R. Metzdrorff,¹ C. Michel,¹⁴ A. Mikami,¹⁶ L. Najera,¹ L. Neuhaus,¹ S. Otabe,⁶ L. Pinard,¹⁴ K. Suzuki,⁶ H. Takahashi,¹⁷ K. Takeda,¹⁶ Y. Tominaga,¹⁶ A. van de Walle,⁷ N. Yamamoto,¹⁸ K. Somiya,⁶ and P.-F. Cohadon¹

AFFILIATIONS

¹Laboratoire Kastler Brossel, Sorbonne Université, CNRS, ENS - Université PSL, Collège de France, Paris F-75252, France

²Department of Physics, The University of Tokyo, Bunkyo-ku, Tokyo 113-0033, Japan

³Institute of Innovative Research, Tokyo Institute of Technology, Meguro-ku, Tokyo 152-8551, Japan

⁴Institute of Space and Astronautical Science, Japan Aerospace Exploration Agency, Chuo-ku, Sagami-hara City, Kanagawa 252-0222, Japan

⁵Research Center for the Early Universe (RESCEU), Graduate School of Science, University of Tokyo, Tokyo 113-0033, Japan

⁶Graduate School of Science and Technology, Tokyo Institute of Technology, Meguro-ku, Tokyo 152-8551, Japan

⁷Université Paris-Saclay, CNRS/IN2P3, IJCLab, 91405 Orsay, France

⁸Department of Physics, Gakushuin University, Mejiro, Toshima-ku, Tokyo 171, Japan

⁹LIGO Laboratory, California Institute of Technology, Pasadena, California 91125, USA

¹⁰Gravitational Wave Science Project, National Astronomical Observatory of Japan (NAOJ), Mitaka City, Tokyo 181-8588, Japan

¹¹Centre de Nanosciences et de Nanotechnologies, CNRS, Université Paris-Saclay, F-91120 Palaiseau, France

¹²Laboratoire Commun de Métrologie (LCM LNE-Cnam), F-93210 La Plaine Saint-Denis, France

¹³Thorlabs Crystalline Solutions, Santa Barbara, California 93101, USA

¹⁴Université Lyon, Université Claude Bernard Lyon 1, CNRS, Laboratoire des Matériaux Avancés (LMA), IP2I Lyon, F-69622 Villeurbanne, France

¹⁵ESPCI, CNRS, F-75005 Paris, France

¹⁶Division of Chemistry, Graduate School of Science, Kyoto University, Kyoto 606-8502, Japan

¹⁷Experimental Quantum Information Physics Unit, Okinawa Institute of Science and Technology, Tancha 1919-1, Okinawa 904-0495, Japan

¹⁸Department of Applied Physics and Physico-Informatics, Keio University, Hiyoshi 3-14-1, Kohoku, Yokohama 223-8522, Japan

Note: This paper is part of the special topic on Quantum Acoustics.

a) Present address: Center for Gravitational Astrophysics, Australian National University, Acton, ACT 2601, Australia.

ABSTRACT

We present a number of approaches, currently in experimental development in our research groups, toward the general problem of macroscopic quantum mechanics, i.e., manifestations of quantum noise and quantum fluctuations with macroscopic (engineered and microfabricated by man) mechanical systems. Discussed experiments include a pendulum, a torsion pendulum, a ng-scale phononic-crystal silicon nitride membrane, a μ g-scale quartz resonator, and mg-scale mirrors for optical levitation. We also discuss relevant applications to quantum thermometry with optomechanical systems and the use of squeezed light to probe displacements beyond conventional quantum limits.

Published under an exclusive license by AIP Publishing. <https://doi.org/10.1116/5.0128487>

I. GENERAL INTRODUCTION: WHY MACROSCOPIC QUANTUM MECHANICS?

Optomechanics is the field of physics that deals with the coupling between the light field and mechanical motion, either by radiation-pressure, the photothermal force,¹ or the gradient force.² Optomechanics has experienced a huge development over the last 25 years, with a number of landmark experiments: feedback cooling of a mirror,³ radiation-pressure cooling,^{4,5} quantum ground state of an optomechanical system,⁶ asymmetry of motional sidebands,⁷ etc. These experiments take advantage of an important feature of optomechanical systems, the ability to couple them to a colder degree of freedom (such as the light field for radiation-pressure cooling) to achieve ground state cooling at temperatures far below their environment. This, together with the unprecedented sensitivity of interferometry to probe displacement, allows to demonstrate at the macroscopic scale quantum mechanical effects usually associated with microscopic systems, such as cold atoms or trapped ions.

This article presents a number of experiments performed in Japanese and French research groups, within the QFilter collaboration jointly funded by JST and ANR, all with the goal of achieving a particular aspect of macroscopic quantum mechanics (MQM), either to demonstrate quantum effects in macroscopic mechanical systems, to take advantage of optomechanical effects to achieve quantum thermometry, or to use squeezed light to probe displacements beyond limits related to quantum fluctuations of the light field. Discussed mechanical systems include a torsion pendulum, a ng-scale phononic-crystal silicon nitride membrane, a μg-scale quartz resonator, and mg-scale mirrors for optical levitation.

II. MULTIPLE PATHS TOWARD MQM

A necessary condition to observe a quantum behavior of a test mass is that the classical noise level of the measurement be sufficiently low compared with the standard quantum limit (SQL). Heisenberg’s inequality reads $\Delta x(t)\Delta p(t) \geq \hbar/2$, which can be translated to $S_x(\Omega) \geq \hbar/m\Omega^2$ ($\equiv S_{SQL}(\Omega)$), with $S_x(\Omega)$ being the power spectrum of the position measurement at the observation frequency Ω .⁸

In a position measurement of a test mass using a laser interferometer as a probe, oscillator thermal noise and mirror thermal noise are major classical noise sources. Let us start from the oscillator thermal noise.

A test mass can be modeled as a damped harmonic oscillator, with a power spectrum of the thermal displacement noise:⁹

$$S_{th} = \frac{4k_B T k \phi}{\Omega [(k - m\Omega^2)^2 + k^2 \phi^2]}, \tag{1}$$

where k_B is the Boltzmann constant, T is the physical temperature, ϕ is the internal mechanical loss, k is the spring constant of the oscillator, m is the mass, and Ω is the measurement frequency. In the case of viscous damping, the internal mechanical loss is replaced by $\gamma\Omega/k$, with γ being the viscous damping rate.

Neglecting the frequency dependence of k and ϕ , one can see from Eq. (1) that the thermal noise level $\sqrt{S_{th}}$ is inversely proportional to $\Omega^{0.5}$ below the resonant frequency of the oscillator $\Omega_0 = \sqrt{k/m}$ and to $\Omega^{2.5}$ above Ω_0 . Since $\sqrt{S_{SQL}}$ decreases with frequency by Ω^{-1} , the oscillator thermal noise level is relatively low above the resonant frequency.

While the oscillator thermal noise is a displacement fluctuation of the test mass, the mirror thermal noise is a sensing noise caused by a deformation of the test mass or of a reflective coating on the surface. In a simplified form with some approximations, the power spectrum of mirror thermal noise is given by^{10,11}

$$S_m = \frac{4k_B T}{\Omega} \frac{1 - \nu^2}{\sqrt{\pi} Y w_0} \phi_m, \tag{2}$$

where w_0 is the beam radius on the mirror, ν is the Poisson ratio, Y is the Young’s modulus, and ϕ_m is the mechanical loss of the mirror substrate. Mirror thermal noise consists of thermal noise of many elastic modes with k of each mode sufficiently higher than the inertial term with the effective mass of each mode. The obtained mirror thermal noise level $\sqrt{S_m}$ is inversely proportional to $\Omega^{0.5}$. Taking both oscillator thermal noise and mirror thermal noise into account, a promising frequency band for the MQM will be limited to $\Omega_1 < \Omega < \Omega_2$, where Ω_1 is the frequency at which oscillator thermal noise reaches the SQL and Ω_2 is the frequency at which mirror thermal noise reaches the SQL; $\Omega_1 < \Omega_2$ is a necessary condition for the quantum measurement.

Let us assume that the spring constant k does not depend on the mass m and the observation frequency Ω is higher than the mechanical resonance $\sqrt{k/m}$. With the increase in the mass, the SQL decreases by $\sqrt{1/m}$, the oscillator thermal noise level decreases by $1/m$, and the mirror thermal noise level stays constant in the simplified expressions. Since Ω_1 decreases faster than Ω_2 with $1/m$, the promising frequency band for the MQM becomes smaller with increasing mass. Testing the MQM is, thus, more challenging with a heavier test mass.

One solution to relax the condition is to introduce an additional trapping mechanism to the damped oscillator. On the right-hand side of Eq. (1), k in the numerator is a part of the structural damping term $ik\phi$ while k in the denominator represents the elastic restoring force. With an additional trapping mechanism that does not introduce an additional damping, only k in the denominator is to be replaced by the new spring constant and the thermal noise level can be reduced. A use of a pendulum is one example. The elastic force of a thin wire is smaller than the gravitational restoring force; $k_{el} \ll k_{gra} \equiv mg/\ell$, and there is no damping force introduced from the gravity. Replacing k in Eq. (1) by $k' \equiv k_{el} + k_{gra}$, we obtain

$$S_{th} = \frac{4k_B T k'}{\Omega [(k' - m\Omega^2)^2 + k'^2 \phi^2]} \frac{k_{el}}{k_{el} + k_{gra}} \phi. \tag{3}$$

The fraction in front of ϕ represents the reduction of the thermal noise level and it is called a gravitational dilution factor. The diluted mechanical loss of the pendulum is approximately given by¹²

$$\phi_p = \frac{k_{el}}{k_{gra}} \phi = \sqrt{\frac{Y_w n \pi d^4}{64 m g \ell^2}} \phi, \tag{4}$$

where Y_w is the Young’s modulus, d is the diameter, ℓ is the length, and n is the number of suspension wires. Reducing the elastic restoring force by using long and thin wires, one can reduce the oscillator thermal noise. This is one approach to test the MQM with a large mass. Practically, however, a required thickness of the wire is as thin as $d \sim 2 \mu\text{m}$ to obtain a significant dilution ($>1/100$) with a milligram-scale test mass.

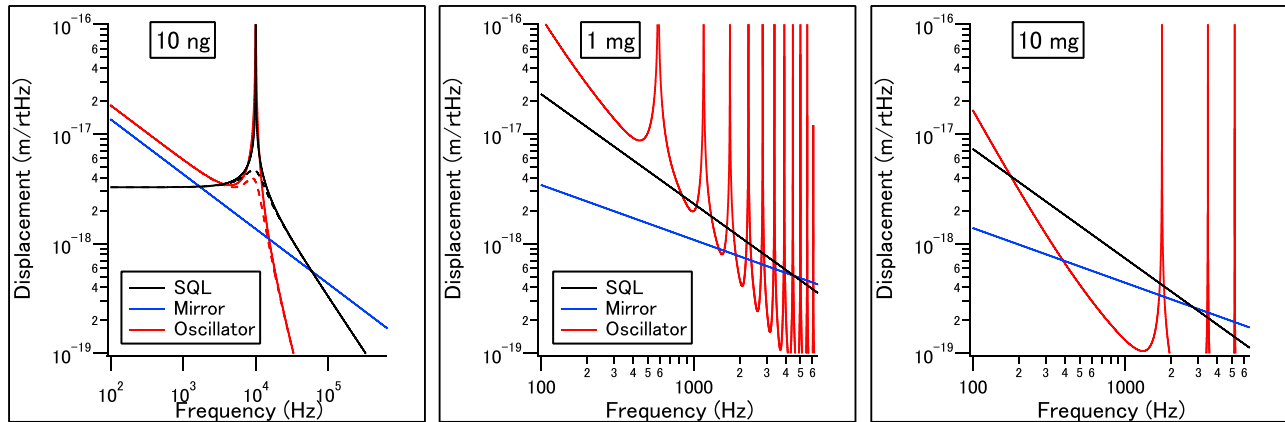


Fig. 1. Thermal noise spectra and SQL of various masses. Left: 10 ng mechanical oscillator. Dashed curves are the oscillator thermal noise spectrum and the SQL with an external control. Center: 1 mg mass suspended by a single-loop pendulum. Right: 10 mg mass suspended by a single-loop pendulum.

Another possible approach to reduce oscillator thermal noise is the levitation of the test mass; no mechanical contact exists between the test mass and the environment. The test mass is trapped by some sort of force (e.g., magnetic, electrostatic, radiation pressure, etc.). If the trapping mechanism does not introduce large fluctuations to the test mass, it is a promising approach to test the MQM. While the gravitational dilution in the pendulum is less significant for the mass lighter than a milligram scale, the levitation approach tends to work well with a light mass.

Figure 1 shows the SQL and thermal noise spectra with a micro-mechanical oscillator (left) and with a pendulum (center and right). Here, we use thermal noise formulae that are more complex and realistic compared with those we have introduced. For the mirror thermal noise, the mechanical loss of the reflective coatings, which is actually larger than the loss in the substrate, is included. The mechanical loss of the substrate is set to 10^{-7} but it is effectively 10^{-5} with the coating loss included. The beam radius on the mirror is set to $\sim 1/5$ of the mirror radius. For oscillator thermal noise, the mechanical loss is set to 10^{-9} , which is challenging but necessary to have the SQL higher than the thermal noise level at the resonance with $m = 10$ ng. For pendulum thermal noise, the violin modes of the suspension wires are included in the calculation. The thermal noise level matches well to the approximated formula at frequencies below the first violin mode, but it deviates from the formula above the frequency. The wire thickness is set to $5 \mu\text{m}$ and the length is 1 cm. The material of the mirror, the oscillator, and the pendulum wire is silica.

In the left panel of Fig. 1, the oscillator thermal noise level is higher than the SQL at the oscillator resonance (solid curves). If we apply an external control to damp the motion at the resonance without introducing extra noise, the thermal noise level becomes lower than the SQL (dashed curves). This technique is called *cold damping*.^{13,14} As mentioned above, the mechanical loss of 10^{-9} we assumed here is quite challenging. The requirement can be relaxed with m .

In the right panel of Fig. 1, the SQL can be reached at around a few hundred Hz. The dilution factor with the 10 mg mass is 47 and the suspension thermal noise level is well suppressed. In the center panel, however, the SQL can be hardly reached. The dilution factor with the 1 mg mass is still as high as 15, but the violin modes come

down to the promising frequencies and the suspension thermal noise prevents the MQM.

The MQM is then not available with a mass in the range between $\sim 1 \mu\text{g}$ and ~ 1 mg, but levitation is promising for a mass in this range. As is summarized in Fig. 2, an appropriate regime to realize the MQM with a mass over a milligram would be to use a pendulum, that with a mass lighter than a micro-gram is to use a good mechanical oscillator, and that with a mass in-between would be to use a levitation technique. There is a technique to reduce thermal noise using a mechanical oscillator with a mass heavier than $1 \mu\text{g}$, and there is an effort to use a pendulum with a milligram scale mass, so the borders of the regimes are still flexible. In our MQM study group, we setup various experimental apparatuses with one of the three regimes. In the following (Secs. III–VIII), we present a number of experiments performed in our collaboration in order to demonstrate SQL-related effects. We also discuss (Secs. IX and X) some related experiments.

III. EXPERIMENTS WITH PLANCK-MASS RESONATORS

To investigate the mass domain around the Planck mass, we have designed a novel resonator shaped as a micropillar¹⁵ shown in Fig. 3(a). For the fundamental longitudinal mode, the displacement

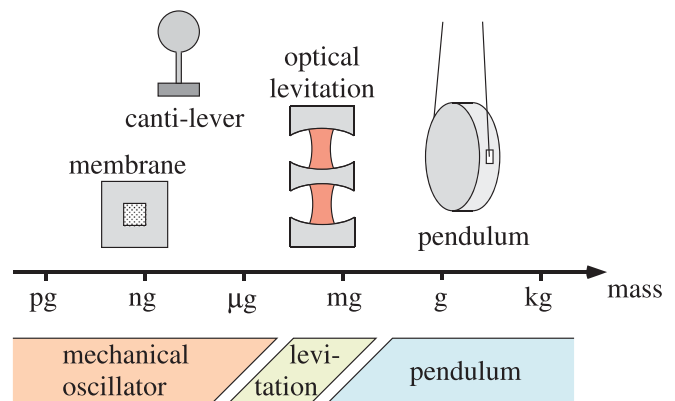


Fig. 2. Three regimes to realize the MQM with different masses.

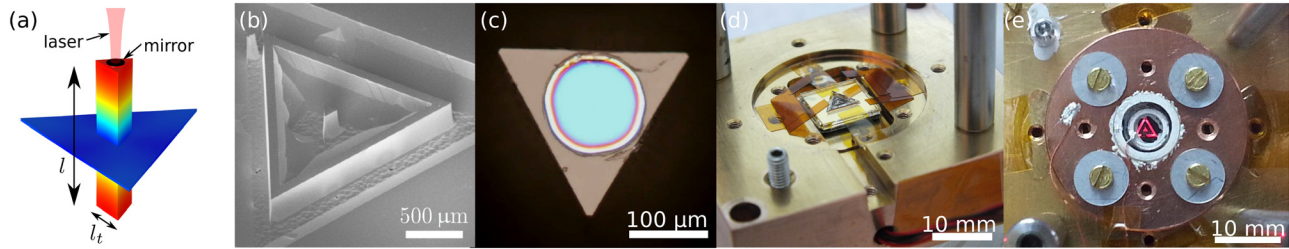


FIG. 3. The mm-scale micropillar. (a) Finite-element modeling of the fundamental vibration mode. Color (from blue to red) indicates total displacement. (b) Scanning electron micrograph of an etched structure, with the additional isolation frame. (c) Optical view of a 100- μ m high-reflectivity mirror coated on one end-face of the micropillar. (d) 1-cm chip clamped inside the optical cavity mount. (e) View of the optomechanical cavity.

profile is predominantly flat across the end face, with the strain gradient along the pillar axis. Such a geometry allows for the clamping of the resonator at a longitudinal node location, and to coat the optical mirror in a stress-free region. Thus, both clamping loss and coating loss are expected to be very low, despite the poor intrinsic mechanical quality factor of the coating layers, and we can expect a mechanical quality factor Q mostly limited by the bulk material's internal losses. To maximize the mechanical quality factor Q of the resonator, monocrystalline quartz is chosen since it has the lowest known intrinsic mechanical loss ($Q > 10^9$) at cryogenic temperatures. With an additional symmetric decoupling frame [see Fig. 3(b)], a Q above 10^6 at room temperature is expected from finite element simulations for this design.

With a pillar length $l \simeq 1$ mm, the resonance frequency of the fundamental compression mode is in the MHz range. As the transverse pillar size l_t must be much larger than the spot size of the laser beam (here in the 10- μ m range) to minimize clipping loss, we have chosen $l_t \simeq 200$ μ m [Figs. 3(c)–3(e)]. The effective mass m is then on the order of $m \simeq 100$ μ g, in the same range as the Planck mass m_P .

Displacement sensing is performed with an interferometric setup shown in Fig. 4. A Nd:YAG laser at $\lambda = 1064$ nm is sent through a triangular filtering cavity, which suppresses its classical phase and intensity fluctuations and provides spatial filtering of the beam. The TEM₀₀

Gaussian mode is mode matched to the high-finesse cavity by focusing lenses. The laser beam is split in two beams: one sent to a homodyne detection scheme, used to feed the feedback loop that lowers the effective temperature of the resonator, the second to a Pound–Drever–Hall (PDH) detection scheme, which provides an independent and out-of-the-loop displacement measurement. With a cavity finesse $\mathcal{F} \simeq 50\,000$ and optical power of a few tens of μ W, both detection schemes have a displacement sensitivity on the order of 10^{-18} m/ $\sqrt{\text{Hz}}$, sufficient to probe the displacement noise at the quantum ground state.

Cooling is performed here with the *cold damping* scheme. The measured displacement signal is used to estimate the resonator's velocity and drive the resonator with an additional damping force, through the radiation pressure force of a modulated beam.³ In the presence of the additional damping, the mechanical resonance gets wider but as the damping is not associated with additional fluctuations (hence the term *cold damping*), it also breaks the usual fluctuation–dissipation theorem. The resonator now is at a lower effective temperature, which depends on the gain g of the feedback loop the resonator displacement is part of. Starting from a base temperature of the resonator of 100 mK, preliminary results displayed in Fig. 5 show that the resonator is cooled down to a temperature around 1 mK, corresponding to a few remaining vibration quanta, which is a limit related to the

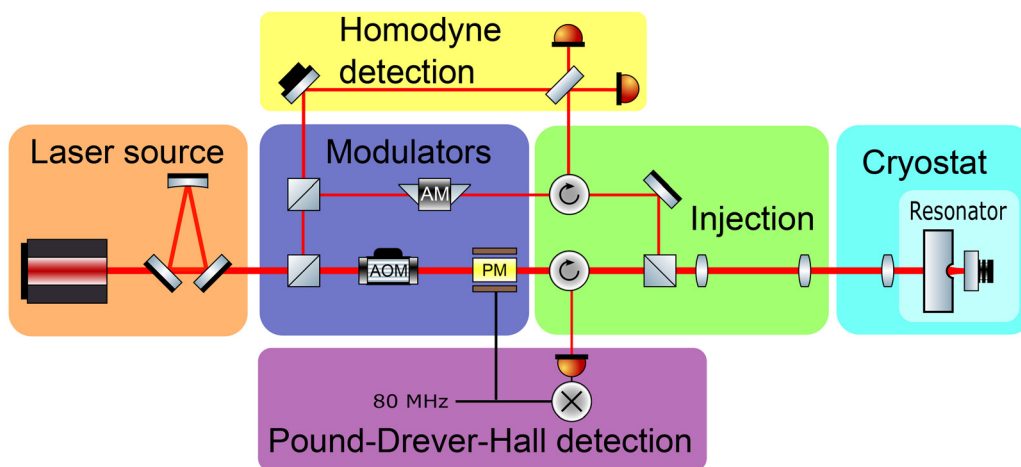


FIG. 4. Experimental setup. A laser source is filtered by a triangular mode cleaner cavity. The beam is modulated at several frequencies by an acousto-optic modulator (AOM), an amplitude modulator (AM) and an electro-optical modulator (EOM). The beam reflected by the cryogenic moving mirror cavity is split in two beams: one sent to a homodyne detection to provide the feedback signal and one to a Pound–Drever–Hall detection scheme for an out-of-the-loop displacement measurement.

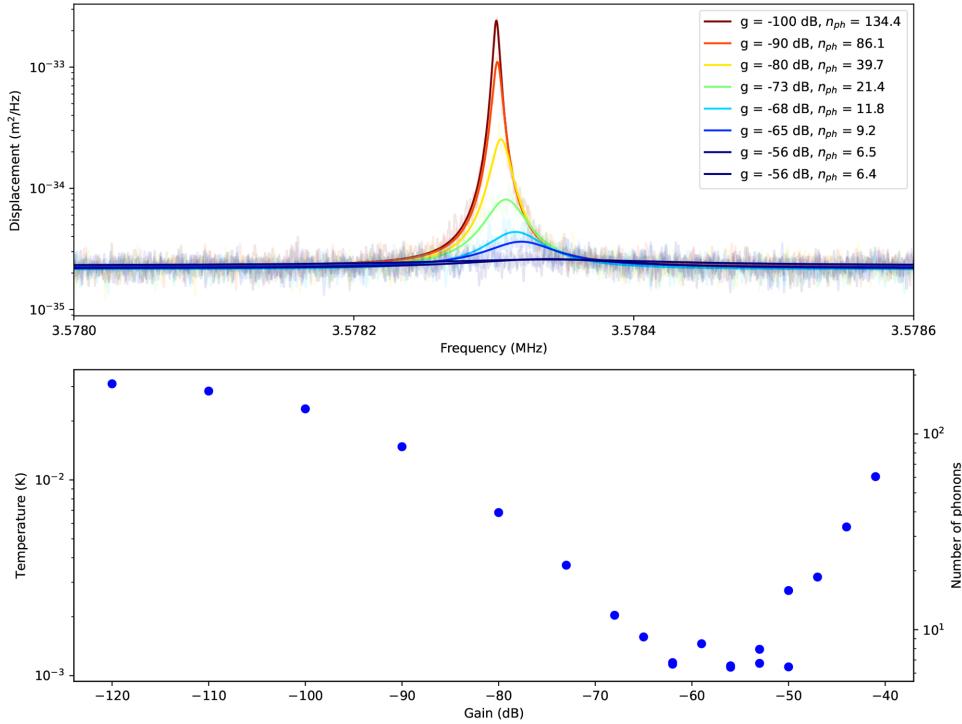


FIG. 5. Preliminary results. Feedback cooling of a 1-mm-long quartz micropillar. Top: Thermal noise spectra, measured for different dampings, measured as gain g of the feedback loop. The different curves correspond to a gain g of -100 (dark red), -90 (light red), -80 (yellow), -73 (green), -68 (light blue), -65 (blue), and -56 dB (dark blue). Bottom: Effective temperature and effective number of phonons versus damping. The phonon number reaches a minimum when the noise curve reaches the measurement sensitivity background.

displacement sensitivity, limited in this frequency range by the background thermal noise level of the cavity input mirror. For larger gains, the setup mostly probes this measurement noise and, as it feeds it back to the displacement, it now increases back the effective temperature.¹⁶

IV. EXPERIMENT WITH SILICON NITRIDE MEMBRANES

Due to their small physical dimensions, ng-scale resonators usually suffer from large surface-losses. It is, thus, challenging to rely purely on the high intrinsic quality factor of crystalline materials to realize ultra-high-Q resonators in this mass-regime. Yet, owing to their large zero-point fluctuations, such systems are very attractive for the demonstration of MQM. They can in particular be used as force sensors,¹⁷ or transducers between otherwise incompatible quantum systems, for instance, microwave and optical photons.¹⁸ Furthermore, a ng-scale resonator coupled to a superconducting circuit has been proposed as a platform to test quantum collapse models on massive quantum superpositions.¹⁹

In spite of the large mechanical loss angle of thin-films, as opposed to bulk materials, suspended membranes²⁰ or strings²¹ of silicon nitride have recently demonstrated $Q \cdot f$ products in excess of 10^{15} Hz, beyond the values achieved with bulk crystalline resonators. These counter-intuitive performances are traceable to a dissipation dilution phenomenon emerging in these high-stress large-aspect-ratio structures.²² In these microscopic resonators, where gravitational energy plays a marginal role, most of the mechanical energy associated with the out-of-plane vibrational modes is stored in the elongation of the film, rather than its bending. In the presence of material damping, defined by a loss angle ϕ , the quality factor of the structure deviates from the intrinsic value $Q_{\text{intr}} = 1/\phi$ by the scaling:²³

$$Q \propto Q_{\text{intr}} \Lambda \quad \text{with} \quad \Lambda = \frac{\sigma l^2}{E h^2}, \quad (5)$$

where the dilution factor Λ depends on the tensile stress of the silicon nitride film σ , the real part of Young's modulus E , l , and h , the lateral extent and thickness of the vibrating film, respectively. For the typical parameters achievable with silicon nitride films ($\sigma \sim 1$ GPa, $h \sim 100$ nm, and $l \sim 1$ mm, $E = 270$ GPa) the dilution factor can exceed 10^5 . In order to reach the ideal scaling of Eq. (5), however, one needs to pay attention to the clamping conditions of the vibrating mode. In particular, the hard-clamping conditions realized in plain membranes or strings lead to a divergence of the bending energy as $\sigma \rightarrow \infty$, and thus a sub-optimal scaling $Q \propto Q_{\text{intr}} \sqrt{\Lambda}$. To reach the scaling of Eq. (5), the technique of soft-clamping can be implemented: it consists in trapping the vibrational mode within the defect of a phononic crystal directly etched within the suspended silicon nitride film.²⁰

In this section, we present our results on softly clamped silicon-nitride membranes realized in a 100-nm silicon-nitride film. The fabrication procedure starts from a commercially available (Si-mat) 2-in. silicon wafer coated on both sides with a 100-nm silicon nitride film of nominal stress 800 MPa. A phononic crystal pattern and rectangular openings are defined by laser lithography on the front and back face of the wafer, respectively. The back face of the wafer is then exposed to a hot KOH solution (85 °C for 210 min) in order to release the phononic crystal membranes using a commercial wafer holder from the company AMMT. The phononic crystal parameters have been chosen to obtain a bandgap covering the frequency range 5.3–6.2 MHz. The defect localized in the center of the phononic crystal is expected to yield a fundamental resonance frequency of 5.69 MHz, a value that is safely within the phononic bandgap of the crystal.

The membranes are characterized at room temperature by spatially resolved laser interferometry. A 2 mW 1064-nm ND:YAG laser is focused on the membrane with a waist of $\sim 9 \mu\text{m}$ and measured by homodyne detection. This setup achieves a quantum-limited detection sensitivity in the 1–10 MHz range of interest. Furthermore, the laser interferometer is mounted on a motorized translation stage allowing us to measure the displacement noise spectrum at any point on the membrane with a spatial resolution of $\sim 9 \mu\text{m}$. The wafer on the other hand is fixed in a vacuum cell at a pressure of $\sim 3 \times 10^{-6}$ mbar to avoid gas damping.

The displacement noise spectrum measured in the center of the defect is presented in Fig. 6(a), together with the expected frequency of the mechanical modes predicted by the Finite Element Modeling software COMSOL. The extent of the bandgap is materialized by the blue region in Fig. 6(b). As expected from the simulations, we observe a large density of peaks corresponding to mechanical modes delocalized over the phononic-crystal outside the bandgap frequency, and a single peak within the bandgap corresponding to the localized defect mode.

We then perform the tomography of the defect mode by monitoring the power spectral density at the defect mode frequency as a function of laser position on the membrane. The mode profile presented in Fig. 6(c) is obtained thanks to a raster scan of the laser over a regular grid of $500 \times 500 \mu\text{m}$ by steps of $5 \mu\text{m}$. The measured mode profile is in excellent agreement with the simulated defect mode profile.

Finally, we extract the quality factor of the defect mode by performing a ring-down measurement shown in Fig. 6(d): the laser intensity is modulated at the defect mode frequency with an electro-optic modulator in order to excite the mechanical mode via radiation pressure. At time $t = 0$, the modulation is switched off and the subsequent decay of the mechanical amplitude $x(t) = x_0 \exp(-\Gamma_m t/2)$ is monitored by demodulating the interferometer signal at the mechanical frequency, yielding a quality factor $Q = \Omega_m/\Gamma_m = 1.17 \times 10^6$. By integrating numerically the curvature of the defect mode, we can deduce the exact value of the dilution factor $\Lambda = 548$ for our particular membrane geometry.²⁴ From this value, we can deduce the intrinsic quality factor of the film $Q_{\text{intr}} = Q/\Lambda = 2136$, a value that is within a factor 2 from that reported previously for thin-films of SiN of comparable thickness.²⁵

Beyond their exceptional mechanical quality factors, silicon nitride membranes can be dispersively coupled to the field of an optical Fabry–Perot with minimal diffraction and absorption losses.²⁶ The advantage of such a modular approach is that the mechanical and optical components of the optomechanical system can be optimized separately. Owing to the ultra-high optomechanical cooperativity achievable, such a system can enter deep into the quantum regime at cryogenic temperatures,¹⁴ and makes a good candidate for room-temperature optomechanics.²⁷ Furthermore, silicon nitride membranes can be functionalized with highly reflective photonic crystals,²⁸

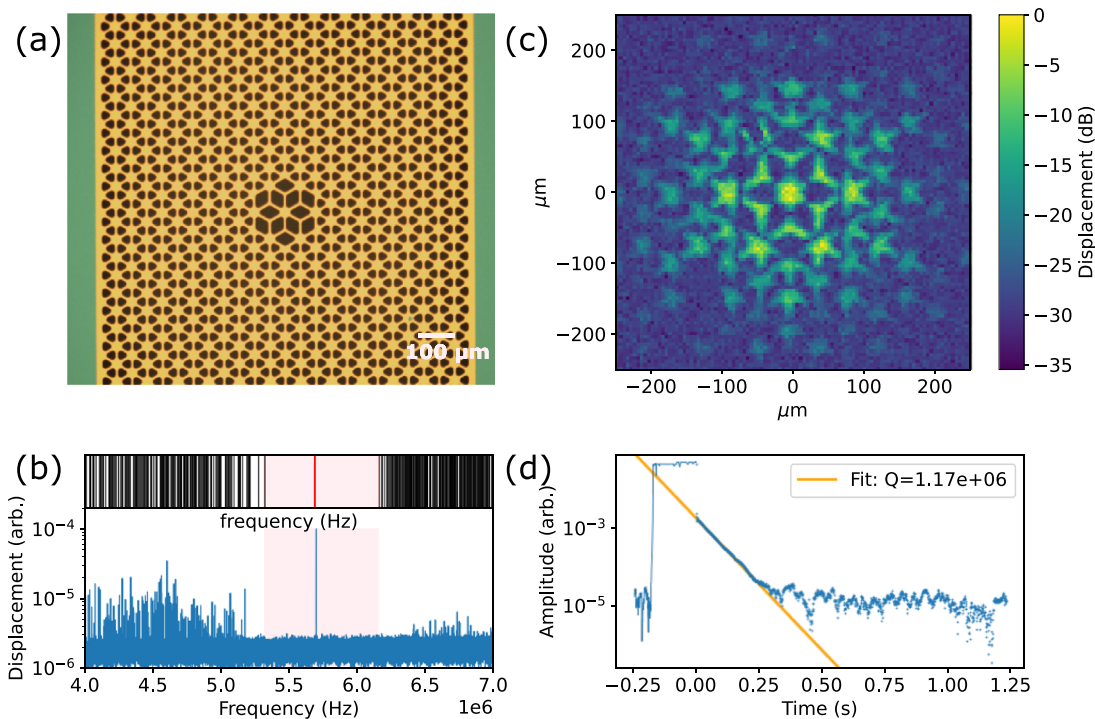


Fig. 6. Room temperature characterization of a high-frequency softly clamped membrane: (a) optical image of a silicon-nitride membrane. In yellow, the silicon-nitride is suspended above air, in green, it is lying above silicon. (b) The upper panel shows the frequencies of the normal modes as predicted by finite element modeling. The lower panel is the thermal displacement noise spectrum measured when the laser interferometer is focused near the center of the defect. (c) Mode profile measurement obtained by raster-scanning the interferometer focus over the surface of the membrane. (d) Ringdown measurement of the defect mode at 5.69 MHz: the mechanical resonator is driven by radiation pressure by a modulating the laser intensity between -0.2 and 0.0 s. The subsequent decay of the vibration amplitude is fitted by an exponential curve yielding $Q = 1.17 \times 10^6$.

allowing for a compact integration into optomechanical force sensors.²⁹ Finally, owing to the phenomenon of dissipation dilution, a thin superconducting layer can be deposited on the membrane, in order to couple it to a superconducting circuit, with modest effect on the mechanical performance.³⁰ Recently, such a functionalized membrane has been cooled close to the quantum ground state by coupling it dispersively to a superconducting microwave cavity.³¹ Such hybrid superconducting/mechanical systems offer a promising route to go beyond Gaussian states of mechanical motion by coupling the mechanical element to a superconducting qubit.¹⁹ Typically, the main challenge in such an experiment is the frequency gap between superconducting qubits operating in the GHz domain, and that of the mechanical element.³² It is, thus, interesting to both raise the mechanical resonance frequency of the mechanical element, and lower the qubit transition frequency. The high-frequency membranes developed in this work—to our knowledge, this is the first time that a softly clamped membrane with a defect mode above 5 MHz is reported on—are thus advantageous in this regard. In parallel, we are also working toward reducing the qubit frequency, as described in an upcoming work.³³

V. MONOLITHIC PENDULUM

As discussed in Sec. II, the dissipation of a pendulum can be greatly reduced by gravitational dissipation dilution. This has allowed pendulum systems to reach the smallest dissipation among various mechanical oscillators so far.³⁴ The dissipation of a state-of-the-art pendulum in table-top experiments is one microhertz, while the dissipation of a state-of-the-art pendulum in large-scale experiments is below 10 nHz. Potentially, the dissipation of a pendulum in table-top experiments can also be reduced to about 10 nHz.

The first challenge for fabricating a low-loss pendulum in table-top experiments is to make a thin, long, and smooth fiber to hang the mass. The radius and length of the fiber determine the dilution factor according to Eq. (4). Furthermore, surface roughness of the fiber should be reduced enough in order to reduce surface loss. Taking these aspects in to consideration, we made a silica fiber of one micron diameter by 5 cm long (right panel of Fig. 7), which gave a material quality factor of 1.2×10^4 and which is close to the surface loss limited Q-factor of $\simeq 2 \times 10^4$ as estimated in Penn *et al.*³⁵ For the case of the milligram scale test mass used in our previous work,³⁴ the length of

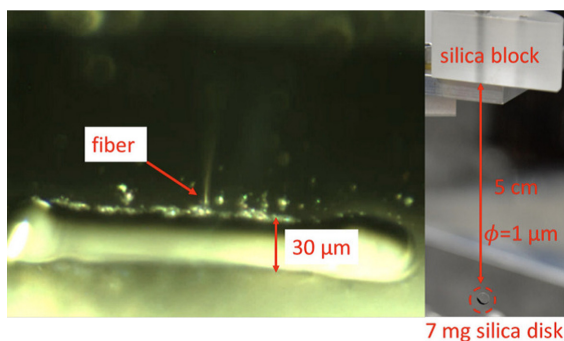


Fig. 7. Picture of the welding point (left) at the mass and overall picture of the monolithic pendulum (right). Reproduced with permission from Cataño Lopez *et al.*, Phys. Rev. Lett. **124**, 221102 (2020). Copyright 2020 American Physical Society.

5 cm was chosen to avoid the effect of higher-order modes (i.e., pitching mode and violin modes) around 100–1000 Hz in displacement measurements.

The second challenge is fixing the fiber to the mass without increasing losses such as clamping and bonding losses. In the case of silica fibers, small losses can be achieved by welding the silica fiber to the silica mirror with a CO₂ laser to achieve a monolithic structure (left panel of Fig. 7). However, for fibers thin compared to the wavelength of CO₂ laser ($\sim 10 \mu\text{m}$), laser welding inevitably damages the surface of the fiber. Due to this welding loss, the current record for dissipation of 1 μHz is still 2 orders of magnitude away from the ideal quality factor given by Eq. (4). This loss could be further reduced by optimization of the shape of the fiber.

In addition to being weldable, silica excels in terms of thermoelastic losses. Since a pendulum cannot be made without physical suspension, the flexing and bending of a pendulum produces spatially inhomogeneous temperature fluctuations in the wire. These fluctuations result in temperature gradients that induce heat flow, which converts vibrational energy into heat. Such a dissipation mechanism is called thermoelastic losses. In general, thermoelastic losses will have two main contributions, one coming from the thermal expansion coefficient, and the other contribution coming from changes in the Young modulus due to temperature variations. The latter is reflected in the fractional change of temperature, also known as the thermal elastic coefficient. There is a possibility of canceling these two terms, as was observed and studied in Bell *et al.*³⁶ For our case, using literature values for fused silica, we see that this cancelation occurs when the diameter of the fiber is around 0.7 μm .

Lastly, let us mention the advantage of a pendulum in terms of linear and continuous displacement measurements. By setting a pendulum at the end of an optical cavity, the displacement can be measured with high spatial resolution (namely, low shot noise). So far, the Brownian motion of the optically trapped pendulum has been measured.³⁷ Measuring the Brownian motion of a low-dissipative oscillator is the first step toward the quantum measurement and control, which is in general difficult to realize. However, such a cavity system including a pendulum can become unstable by optical torque in a cavity.³⁸ To avoid the instability for yaw motion, we proposed to use a triangular cavity, in which the sign of optical torque becomes positive.^{39,40} Thanks to both the high sensitivity coefficient of the optical cavity and the stability of the optomechanical pendulum, it is possible to achieve sensitive measurements with sufficiently low noise to reach the standard quantum limit.³⁴ Combined with the optical spring effect, such a quantum-noise-limited system can be used to generate a quantum entanglement between two pendulum modes in the interferometer.⁴¹

VI. TORSION PENDULUM

A torsion pendulum is one of the most sensitive displacement and force detectors. It has been used as the platform of precision experimental physics, such as measurement of the Newtonian gravitational constant,⁴² tabletop tests of the equivalence principle,⁴³ and tests of the inverse-square law of gravity.⁴⁴ In recent years, the ability to enhance the sensitivity of the readout by integrating mechanical oscillators with optical cavities within the field of cavity optomechanics has renewed interest in fundamental tests of quantum mechanics,⁴⁵ decoherence mechanisms,^{46–50} and gravitational physics using tabletop mechanical experiments.^{51–55} In general, optomechanical experiments

to test several of these proposals call for low-frequency, massive mechanical oscillators measured with a high sensitivity. In this context, a macroscopic torsion pendulum coupled to an optical cavity for enhanced optical readout and control affords a unique combination of capabilities that could enable quantum state preparation in the future.

One of advantages of the torsion pendulum is the low thermal fluctuation because of the low mechanical resonant frequency. At free mass regime, where the frequencies are much higher than the mechanical resonance, the thermal noise spectrum in Eq. (1) can be rewritten as

$$S_{th} = \frac{4k_B T \omega_m^2 \phi}{m \Omega^5} \quad (6)$$

decrease quadratically with the mechanical resonance, in contrast to the linear dependence on the loss angle and temperature. Thus, a low-frequency torsion pendulum can efficiently offset the benefits of high quality factor and cryogenic operation. Since the restoring torque of a single suspension wire is proportional to the radius of the wire to the fourth power, the resonant frequency of a torsion pendulum can be dramatically decreased by using ultrathin suspensions. It should be noted that the benefit of the factor ω_m/Ω derives from the structure damping, not viscous one.

Another advantage is that the optomechanical torsion pendulum has the larger quantum cooperativity than the simple pendulum because of the geometrical characteristic. Here, we compare the displacement of the pendulum with the mass of m read out by a cavity with circulating power of P_{circ} at the center of the mass, and the torsion pendulum read out by two cavities with circulating power of $P_{circ}/2$ at each edge. Defining the geometrical factor a as $a \equiv I/(md^2)$, where I and d are the inertial moment and length of the torsion pendulum, respectively, the quantum cooperativity is enhanced by a factor of $1/(4a)$,⁵⁶

$$\mathcal{C}_{qu}^{tor} = \frac{1}{4a} \mathcal{C}_{qu}^{pen}. \quad (7)$$

This factor is over unity in any torsion pendula, e.g., $a = 1/12$ with a torsion pendulum whose mass is uniformly distributed along d . Therefore, even with the same damping rate of the oscillator, the torsion pendulum can be operated easily in quantum regime. In addition, the differential readout of the two cavities leads to suppression of the longitudinal noises of the torsion pendulum such as the pendulum thermal noise and the seismic noise.

A milligram-scale optomechanical torsion pendulum has been successfully developed with two optical cavities situated on either end of the bar mirror.⁵⁷ An experimental schematic picture is shown in Fig. 8. The torsion pendulum we use is formed by suspending a 10-mg bar mirror (silica substrate of dimensions $15 \times 1.5 \times 0.2 \text{ mm}^3$) on a carbon fiber that is $\sim 6 \mu\text{m}$ thick and 2.2 cm long. The small diameter and low shear modulus of the fiber ($\sim 10 \text{ GPa}$) give a low torsional resonant frequency $\omega_m/(2\pi) = 90 \text{ mHz}$, while ringdown measurements indicate a damping rate of $\gamma_m(\omega_m)/(2\pi) = 35 \pm 3 \mu\text{Hz}$, corresponding to a quality factor of $Q_m = (2.6 \pm 0.2) \times 10^3$. The two cavities have a triangular configuration to prevent radiation pressure torque instabilities.⁴⁶ Their input mirrors, half inch in size with reflectivity $R_i = 99.8\%$, are mounted on a holder on picomotors to allow for cavity alignment. The second mirror, with the similar size but the different reflectivity of $R_c = 99.99\%$ is placed in a brass spacer weighing 70 g in total, and suspended from four piano wires. A coil-magnet actuator is used to control the cavity length. The cavities are each driven by 20 mW of 1064-nm light from a Nd:YAG laser derived at a beam splitter. Either cavity is designed to be 9 cm long, and their finesse was measured to be $\mathcal{F}_A = (3.0 \pm 0.3) \times 10^3$ and $\mathcal{F}_B = (2.4 \pm 0.2) \times 10^3$, respectively, which results in the circulating power of around 10 W. The two signals of the amplitude fluctuation of light reflected from each cavity are detected on a PD and subtracted to obtain the rotational motion of the torsion pendulum.

The measured torque spectral density is shown in Fig. 9 with various budgeted noises. The peak sensitivity of $2 \times 10^{-17} \text{ N m}/\sqrt{\text{Hz}}$ (corresponding to an angular displacement of $10^{-15} \text{ rad}/\sqrt{\text{Hz}}$) around 100 Hz is the best torque sensitivity achieved at the milligram scale.

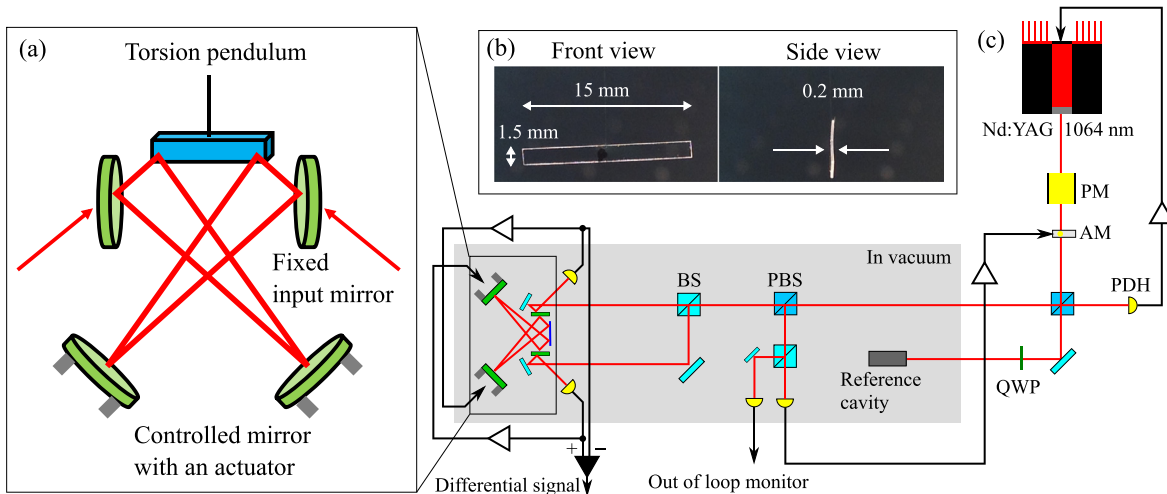


Fig. 8. (a) Configuration of the torsion pendulum with two triangular cavities, one on each edge of the bar, used for readout. Input mirrors for either cavity are rigidly mounted, while the third mirror is suspended and can be actuated for cavity length control. (b) Pictures of the bar mirror from front and side views. (c) Simplified schematic of the experiment.

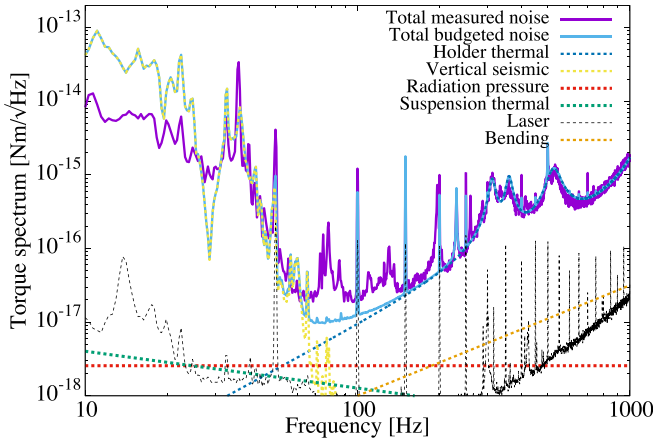


Fig. 9. Noise spectra of differential force on the ends of the bar mirror, calibrated as a torque. The measured spectrum (purple) can be largely understood using a noise budget (cyan) consisting of vertical seismic noise (yellow dotted), thermal noise of the input mirror holder’s structural modes (blue dotted), laser noise (black dotted), internal bending mode of the bar mirror (orange dotted), thermal noise from the pendulum suspension (green dotted), and quantum radiation pressure torque noise from the readout cavity modes (red dotted).

Fundamental noises related to the pendulum, such as suspension thermal noise of the torsional mode, and quantum radiation pressure noise, are shown as the green and red dotted lines, respectively. The quantum radiation pressure torque noise is given by

$$S_{\tau}^{\text{rad}}(\Omega) = \frac{2\hbar}{\delta} \omega_{\text{eff}}^2 L_{\text{eff}}^2, \quad (8)$$

where δ is the cavity detuning normalized by the cavity line width, and ω_{eff} is the effective resonant frequency including the optical spring. In our experiment, these are measured to be $\delta \sim 0.6$ and $\omega_{\text{eff}}/(2\pi) \sim 1$ kHz. The resulting estimate for the quantum radiation pressure torque noise contributes about $(14 \pm 3)\%$ to the measured spectrum around 100 Hz. This value, along with our previous work,³⁷ is an improvement on other reports on milligram- and gram-scale experiments to observe quantum radiation pressure noise.^{58–60}

While contribution of the quantum radiation pressure fluctuation is small, two dominant noises are observed in the torque spectrum. One is the vertical seismic noise (cyan dotted) measured independently by a seismometer. It limits the sensitivity at low frequencies (<50 Hz) where the seismometer and the cavity length signals have a coherence close to unity. The other is the thermal noise of the input mirror holder (brown dotted) limiting the sensitivity at high frequencies (>150 Hz). The non-monolithic construction of the input mirror holder, partly because of the various moving components for cavity alignment, has several structural resonances which we model using their quality factors (typically below 10) and resonant frequencies. A more fundamental but small contribution to the noise budget at these frequencies is due to the thermal motion of the bending mode of the bar mirror substrate (orange dotted). At last, torque-equivalent laser noise (black dotted) arising from residual amplitude and frequency noise limits the readout sensitivity (in reflection measurement for detuned operation), while it remains smaller. Despite accounting for all the above sources of noise, an unexplained excess remains in the

50–150 Hz interval; we conjecture that the excess is due to coupling with the stray scattering in the cavity.

Given the result of the sensitivity, replacing the triangle cavities with two linear cavities has the potential to improve the sensitivity at high frequencies. The linear cavity can be built with a mirror on the edge of the torsion pendulum and a suspended input mirror. Thus, the thermal noises concerning the input mirror holder can be avoided. An obstacle with a suspended linear cavity is about the instability of its rotational degree of freedom. The suspended mirror can be unstable due to the radiation pressure inside the cavity.³⁸ This instability is called Sidles–Sigg instability, and one of the two modes in a rotational direction is unstable. To overcome Sidles–Sigg instability, we proposed to construct a linear cavity in the negative- g regime with a test mass mirror that is much lighter than the input mirror. In the negative- g regime, where the curvatures of the cavity mirrors are longer than the cavity length, the common mode rotational motion can be unstable by increasing the laser power. However, the common mode can be mechanically stiff enough by using the heavy input mirror. Two characteristics of the negative- g regime and the unbalanced mass mirrors, Sidles–Sigg instability, is surmounted.

We have succeeded in validating this configuration experimentally by using an 8 mg mirror as the test mass.⁶¹ The result shows that the rotational degrees of freedom was stabilized with an increase in the intracavity power as the theoretical calculation predicted, while the common mode remained stiff. With these results, we plan to replace the triangular cavities on the torsion pendulum with the linear cavities. Accordingly, the newly designed torsion pendulum consists of two 8 mg mirrors, whose interval is connected by a glass pipe; the form of the torsion pendulum is similar to a dumbbell.

VII. OPTICAL LEVITATION

Mechanical oscillators discussed so far are supported by some sort of mechanical structures with finite mechanical loss. Trapping oscillators with an optical spring can greatly dilute the mechanical loss, and its ultimate example is to trap an oscillator by the optical field alone. Since the invention of optical tweezers by Ashkin in 1970s, optical tweezers have been used in a wide range of fields to levitate nanoscale to microscale particles that are transparent to laser beam. In more recent years, there have been numerous experimental and theoretical efforts to probe quantum physics with levitated optomechanical systems. The ground state cooling of levitated nanoparticles has been already demonstrated by several groups.^{62–64}

Since optical tweezers require optical gradient force in a highly focused laser beam, the size of the levitated particle has to be smaller than the size of the beam. Therefore, optical tweezers can levitate particles which has the mass of only up to nanogram scales. To levitate even more massive objects, optical levitation of a highly reflective mirror with vertical optical cavities have been recently proposed and studied.^{65–67} The levitated mirror and the mirror at the bottom form a cavity, and the levitated mirror is supported by the radiation pressure of the intracavity field. The intracavity power required to levitate a mirror can be easily calculated with

$$P_{\text{circ}}^{\text{lev}} = \frac{mg_{\text{grav}}c}{2}, \quad (9)$$

where $P_{\text{circ}}^{\text{lev}}$ is the sum of all the power on the levitated mirror projected to the vertical axis, m is the mass of the levitated mirror and g_{grav} is the

the original restoring torque of the pendulum, we used an ultrathin tungsten wire to suspend the pendulum. The length of the wire was 105 mm and the radius was 20 μm . Consequently, the original resonant frequency of the torsion pendulum was 32.2 ± 1.1 mHz, which was small enough to measure the optical restoring force. The cavity was built with the quarter-inch mirror attached to the torsion pendulum and the half-inch input mirror. The laser beam of wavelength 1550 nm was injected, and the finesse of the cavity was measured to be 880 ± 90 . The horizontal restoring force on the mirror was reflected to the resonant frequency of the pendulum. Therefore, we measured the resonant frequency to estimate the optical restoring force. The resonant frequency was precisely determined by measuring the transfer function of the pendulum. Since the rotational angle of the torsion pendulum was feedback controlled by using the coil-magnet actuators and the angle sensor with the optical lever, the transfer function could be measured by injecting the reference signal into the feedback loop.

We observed that the resonant frequency shifts toward high when the laser beam was on, and it was consistent with the theoretical model. The measured restoring force due to the sandwich configuration is shown in Fig. 12. From the result, we concluded that the sandwich configuration actually stabilized the horizontal motion of the mirror.

Studies on the fabrication of milligram-scale mirrors for the optical levitation is also being done. The challenge is to add a curvature on the mirror, and our group have been working on fabricating a 3 mm diameter fused silica mirror curved from a stress from a high reflective coating. This coating on one side will act as a high reflective coating for both sides and can be used in the sandwich configuration. In 2021, we have successfully fabricated such a mirror (Fig. 13), and the radius of curvature was measured to be around 500 mm. We initially used a substrate with 1-in. diameter and deposited a high reflective coating,



FIG. 13. A prototype 2-mg fused silica mirror with a diameter of 3 mm and a thickness of 0.1 mm. A high reflective coating with a thickness of around 6 μm and a transmission of 10 ppm is deposited.

and then proceeded to cutting the coated substrate to 3 mm diameter. To levitate a mirror with Fabry-Pérot cavities of centimeter scale lengths, a similar length is required for the radius of curvature. We are now working on depositing thicker coating on thinner substrate to make the radius of curvature smaller. Stoney's equation states that the radius of curvature is inversely proportional to the coating thickness and the square of substrate thickness.⁶⁹

VIII. DIAMAGNETIC LEVITATION

A rather well-known levitation method is a magnetic levitation. The magnetic levitation technique is used, for example, in a vacuum pump flywheel or in a high-speed ground transportation.⁷⁰ Drever proposed to use a magnetic suspension system in a gravitational wave detector.⁷¹ The system consists of a pair of oppositely poled magnets attached to a test mass, a pair of long fixed magnets, sensors and a servo to stabilize the levitation. Giazotto proposed to use an electrostatic levitation system in a gravitational wave detector, noting a low noise coupling compared with the magnetic levitation.⁷² The system also requires an active servo control.

In the case of the levitation using two permanent magnets, Earnshaw's theorem prevents the stability in the horizontal directions,⁷⁰ but it does not apply to the diamagnetic levitation. The measure of the magnetic susceptibility in a diamagnetic material is much lower than that in a ferromagnetic material; see Table I. In addition, some diamagnetic materials are not suitable for the MQM as the electrical conductance is high and it can lead to large excess thermal noise through the eddy current damping. We chose to use fused silica for

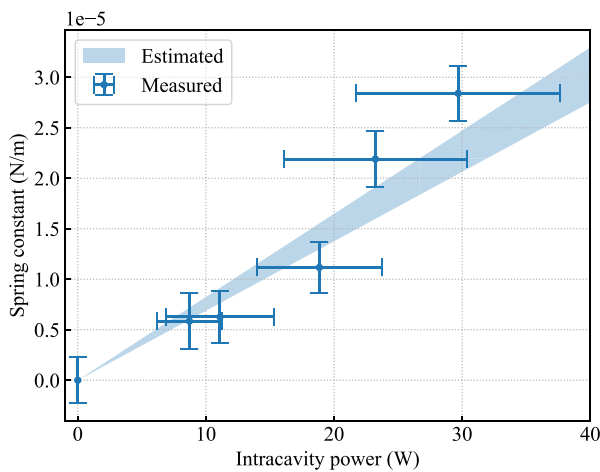


FIG. 12. Spring constant corresponding to the optical restoring force due to the sandwich configuration. First, we measured the restoring force of the torsional pendulum itself. The data point with zero intracavity power corresponds to this measurement. Then, we injected the laser beams with different powers. The other five points represent the results with the laser on. The increase in the restoring force is clearly observed, and it was consistent with the theoretical prediction. Reproduced with permission from Kawasaki *et al.*, Phys. Rev. A **102**, 053520 (2020). Copyright 2020 American Physical Society.

TABLE I. Volume magnetic susceptibility χ_v and electrical conductivity σ of some materials.

	χ_v	$\sigma(\Omega\text{m})$
Iron	2×10^5	1×10^7
Graphite	-2×10^{-4}	$2 \sim 4 \times 10^5$ (basal plane) 3×10^2 (perpendicular)
Bismuth	-1.6×10^{-4}	8×10^5
Water	-9.0×10^{-6}	0.005–0.5
Fused silica	-1.4×10^{-5}	1×10^{-16}
Diamond	-2.2×10^{-5}	1×10^{-12}

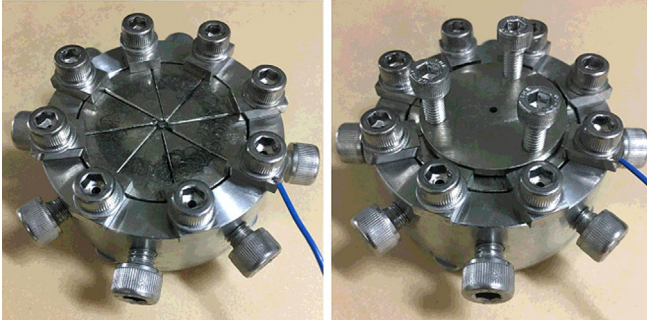


FIG. 14. A magnet levitation system. Accommodated in the stainless container are eight magnets in a cheese-cake shape with the magnetic pole directing inward and an iron bar at the center (left). An iron plate covers the top of the system to create a strong magnetic gradient (right). Reproduced with permission from Nakashima, *Phys. Lett. A* **384**, 126592 (2020). Copyright 2020 Elsevier.

the test mass. The negative magnetic susceptibility is decent compared with graphite or bismuth but it is possible to levitate it with a permanent magnet array.

The condition to balance the gravity and the magnetic force is given by

$$B_z \frac{\partial B_z}{\partial z} = \frac{\mu_0 \rho g}{\chi}, \quad (10)$$

where B_z is the magnetic field in the z -direction, μ_0 is the magnetic permeability, ρ is the density, g is the gravitational acceleration, and χ is the magnetic susceptibility per volume. Since the magnetic susceptibility is low for fused silica, we must increase B_z or $\partial B_z / \partial z$ to levitate the mass. Note that the mass does not appear in the equation but the system needs to be small to increase the magnetic field gradient.

In 2019, we succeeded in levitating a 1-mg fused silica bulk using a permanent magnet array shown in Fig. 14. The cylindrical magnet array consists of eight magnets in a cheese-cake shape with the magnetic pole directing inward of the cylinder. There is a space at the

center of the cylinder and an iron bar is accommodated. An iron plate with a hole at the center is on top of the cylinder. The magnetic field concentrates to the iron bar and goes up toward the iron plate to change the direction to outward. This structure realizes a large magnetic field gradient in the vertical direction.⁷³ At the time, we did not have such a small polished fused silica mirror, and could not measure the actual thermal noise level. In 2020–2021, we successfully developed a 2-mg fused-silica flat mirror, cut, polished, and coated by *Sigmakoki Co., LTD*. The diameter and thickness of the mirror are 1.5 and 0.6 mm, respectively. The surface accuracy is $\lambda/10$ and the nominal reflectivity is $\geq 99.9\%$. In order to levitate the 2-mg mirror, we slightly modified the magnet system from the original one;⁷³ the cross-sectional view of the magnetic field in the updated system is shown in Fig. 15.

The entire system was put in a vacuum chamber and the dissipation was measured with a ring-down measurement. Currently, the measured Q value is on the order of 10 000. We are trying to reduce the environmental couplings, such as seismic vibrations and residual gas damping, aiming at a Q value of 1×10^6 or higher to reach the standard quantum limit.

IX. OPTOMECHANICAL THERMOMETRY

The redefinition⁷⁴ of the kelvin in 2018 is based on a fixed value of the Boltzmann constant k_B . Consequently, the metrology community is encouraged to put strong efforts into the dissemination of the thermodynamic temperature for the mise-en-pratique of the kelvin. Moreover, there is a strong demand on sensor technology able to cover a wide range going from cryogenic (below 1 K) up to room temperature (300 K), adapted to advanced manufacturing metrology like “lab on a chip,” microelectronics, optoelectronics or microfluidics. New temperature sensors based on photonics or optomechanics are good candidates⁷⁵ to answer these metrology challenges as they offer nanoscale spatial resolution, large temperature range, and additionally can be self-calibrated with noise-thermometry and even provide a path toward primary temperature standards using quantum measurements.⁷⁶

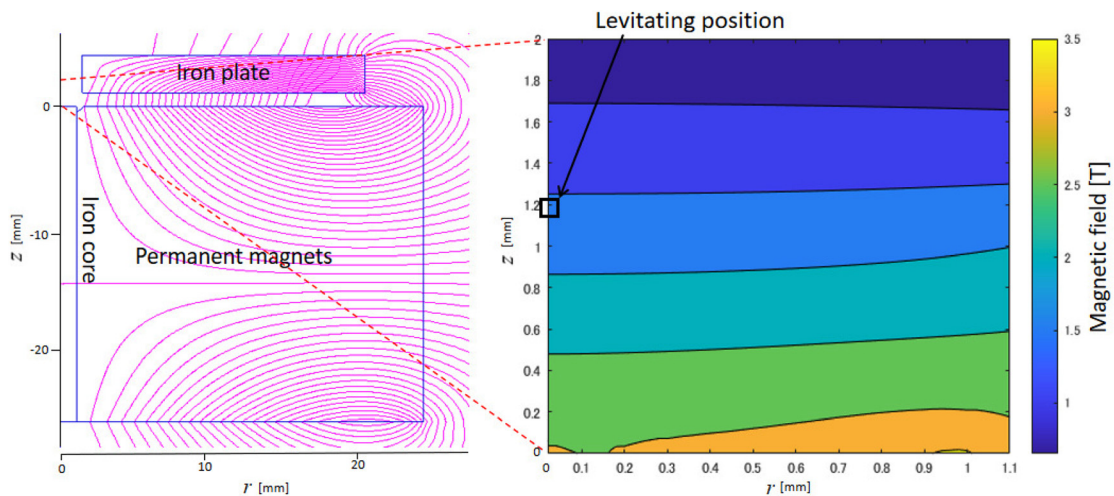


FIG. 15. A magnetic field in the current magnetic system.

In this section, we present preliminary results obtained with optomechanical sensors, which combine the ability to realize photonic thermometry and mechanical noise-thermometry and can be further optimized to work in the quantum regime, thus providing a sensor working on a large range of temperature with the ability to a self-calibration.

The optomechanical crystal is made of a 200-nm-thick GaP (refractive index $n = 3.1$) suspended nanobeam cavity, 700 nm wide and approximately 20- μm -long waveguide. A ladder-like optical cavity is then performed by drilling holes with a diameter of 260 nm periodically positioned along the waveguide. At the center of the nanobeam cavity, the lattice constant ($a_{\text{center}} = 410 \text{ nm}$) is chosen in order to allow a propagating mode at the targeted wavelength (around 1550 nm). From the center to the end of the nanobeam, periodicity is gradually increased till a position where the period is kept constant ($a_{\text{end}} = 480 \text{ nm}$). In both end regions, the crystal acts as a Bragg mirror, and the whole structure behaves like a short Fabry Perot cavity.

The concept of a photonic thermometer is to guide and confine light into a photonic crystal resonator which presents optical resonances when the effective optical length of the cavity is a multiple m of the half wavelength,

$$\frac{\lambda_m}{2} = \frac{n(T, \lambda)L_{\text{eff}}(T)}{m}, \quad (11)$$

where n is the refractive index, L_{eff} the effective length of the cavity which takes into account the penetration of light into the Bragg mirrors, and T the temperature. Due to thermo-optic effect both L_{eff} and n have a strong temperature dependency resulting in an optical resonance frequency shift.

To perform photonic thermometry, the photonic crystal resonator is attached on a copper mechanical part equipped with calibrated Cernox thermometers and inserted into a circulating Helium cryostat. White light from a superluminescent diode is coupled into the sample and collected back, with a lensed optical fiber. The reflected light monitored with an optical spectrum analyzer is presented on Fig. 16 for temperatures ranging from 300 K down to 4 K. The optical resonances are characterized by a clear dip in the reflection spectrum due to absorption of the resonant light in the photonic crystal or transmission through it to the bulk. The resonance frequency shift exhibit a good linearity with respect to temperature down to 100 K with a slope of -7.05 GHz/K . As mentioned previously, this effect is mainly due to the modification of the refractive index of the material with temperature ($\Delta n/\Delta T/n \simeq 3 \times 10^{-5} \text{ K}^{-1}$ for GaP) and, at a lower level, to the thermal expansion of the structure ($\alpha < 4 \times 10^{-6} \text{ K}^{-1}$ for GaP). Below 100 K, the linearity is broken due to the expected saturation of thermodynamical constants of the material.

The basic concept of noise thermometry is to monitor the thermomechanical noise caused by the Brownian thermal motion of an harmonic oscillator and infer the temperature with the equipartition theorem relation $\langle x^2 \rangle \propto k_B T$ between the displacement x of a single mechanical mode and the temperature of the thermal bath T . This technique is similar to Johnson noise-thermometry, which has been extensively studied for the determination of the Boltzmann constant.⁷⁷ The optomechanical crystal was designed to have localized mechanical modes with a fundamental mode at 2.8 GHz. A tunable laser beam's frequency is kept on the photonic crystal's optical mode resonance, and the phase of the output beam is monitored with a homodyne

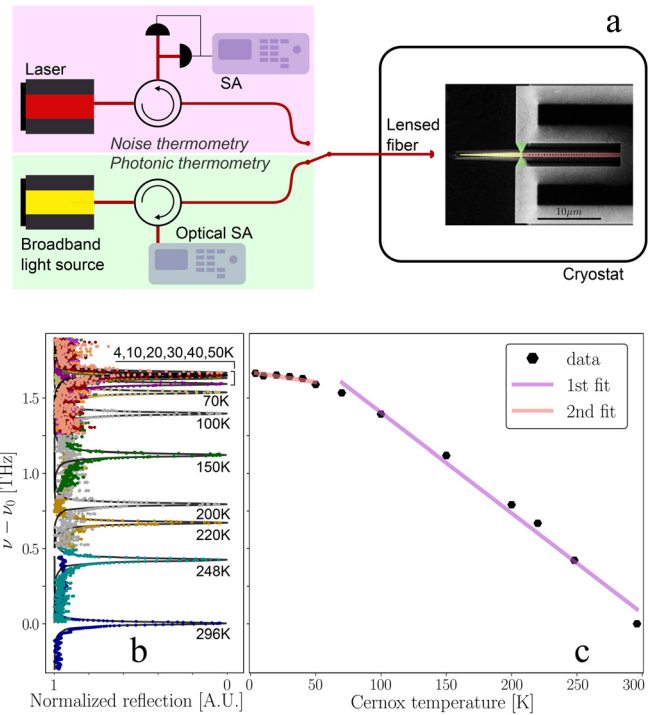


Fig. 16. Photonic/phononic thermometry. (a) Simplified optical setup for performing the photonic and optomechanical noise thermometry. (b) Optical spectra of the photonic crystal cavity at different temperatures ranging from 296 to 4.2 K. Superimposed to the data points in black solid lines are Lorentzian fits. (c) Fit extracted optical resonance frequency ν_0 plotted against the Cernox temperature reading. The data points are fitted with two linear fits, in purple and orange.

detection. Figure 17(a) displays the displacement noise spectra $S_{xx}(\Omega)$ for $T = 296, 70,$ and 4 K where one can see the different mechanical modes in black dots and superimposed to it, in orange solid lines, a fit of these data. The area below the fundamental mode (highlighted in

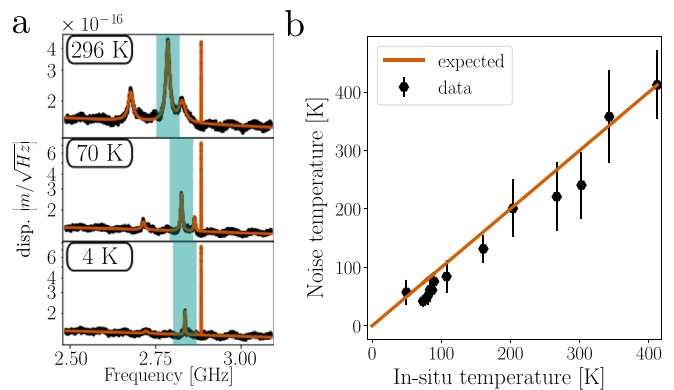


Fig. 17. Noise thermometry results. (a) Displacement noise spectra of the resonator acquired at $P_{\text{in}} = 100 \mu\text{W}$ in black dots and fits to the data in orange solid lines for various temperatures. The fundamental mechanical mode is highlighted in blue. (b) Noise temperature extracted from the calibrated area of the fundamental mode (in black) plotted against the sample's estimated temperature via photonic thermometry. The expected behavior is plotted in orange solid line.

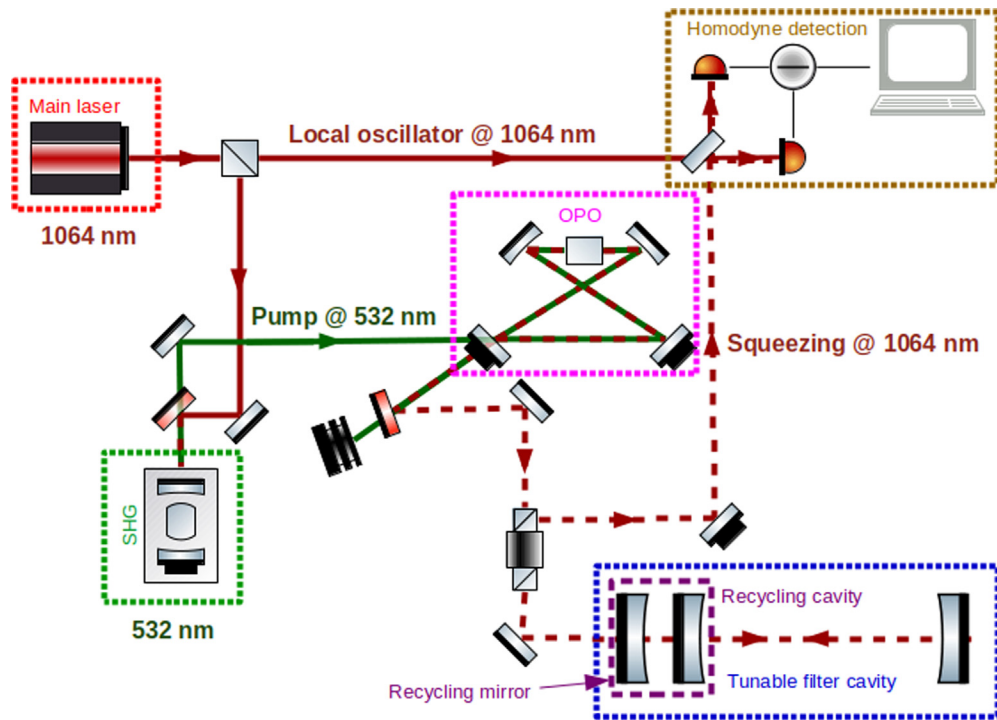


Fig. 18. Simplified scheme of principle of the experiment to test frequency-dependent squeezed light with a tunable corner frequency. The squeezing is generated inside the OPO, sent into the filter cavity to become frequency-dependent, and then measured on the homodyne detection by combination with a local oscillator.

blue) is computed and normalized by the detection’s sensitivity for cryostat temperatures ranging from 300 to 4 K. The noise inferred temperature is depicted in Fig. 17(b) as a function of the sample’s temperature estimated with the photonic thermometry method. Indeed, the noise spectra were acquired with an input laser power $P_{in} = 100 \mu\text{W}$ inducing self-heating in the sample due to light absorption. This effect results in a strong asymmetry and even a bistable behavior of the optical resonance as the resonance frequency shifts away as light is coupled into the cavity. Consequently, the sample’s effective temperature can be higher by tenths of kelvin compared to the base plate. However, temperature measured by both noise and photonic thermometry is in good agreement as both methods probe the effective sample’s temperature and not that of the surrounding thermal bath.

X. BEYOND THE SQL: PROBING MOTION WITH FREQUENCY-DEPENDENT SQUEEZED LIGHT

Terrestrial interferometric gravitational-wave detectors are probing the motion of kg-scale test masses to detect the passage of gravitational waves. Quantum noise is one of the main limiting noise sources of these detectors with radiation-pressure fluctuation noise at low frequencies and shot noise at high frequencies. The frequency f_{SQL} at which both noises are equal depends on the laser power used inside the interferometer.⁷⁸ When using frequency-independent squeezing for gravitational-wave detectors,⁷⁹ we usually reduce quantum noise in the phase quadrature at the cost of increasing it in the amplitude quadrature. However, the use of frequency-dependent squeezing with an appropriate corner frequency f_c , to transition from phase squeezing at

high frequencies to amplitude squeezing at low frequencies, enables to beat the SQL.⁸⁰

The corner frequency f_c of frequency-dependent squeezing is given by the parameters (length and finesse) of the filter cavity in which the squeezed photons are sent to obtain frequency-dependent squeezing. To be optimal, the corner frequency f_c must be close to f_{SQL} which depends on laser power. Thus, a filter cavity with tunable parameters could be interesting to follow the power change of the interferometer and keep optimal conditions for frequency-dependent squeezing.

A simplified experimental scheme of a smaller-scale experiment under test,⁸¹ with a 50-m long filter cavity, is shown in Fig. 18. The squeezed light at 1064 nm is produced within a nonlinear optical

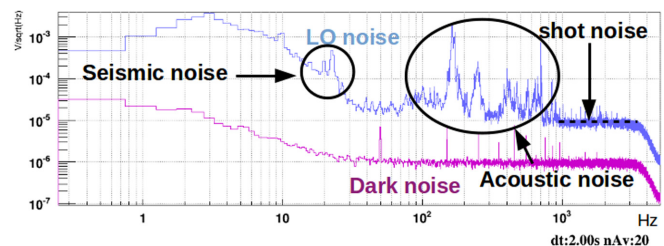


Fig. 19. Dark noise and local oscillator noise on the homodyne detection signal. The local oscillator noise shows seismic and acoustic noise below 1 kHz and shot noise between 1 and 3 kHz, which is 1 order of magnitude higher than the dark noise.

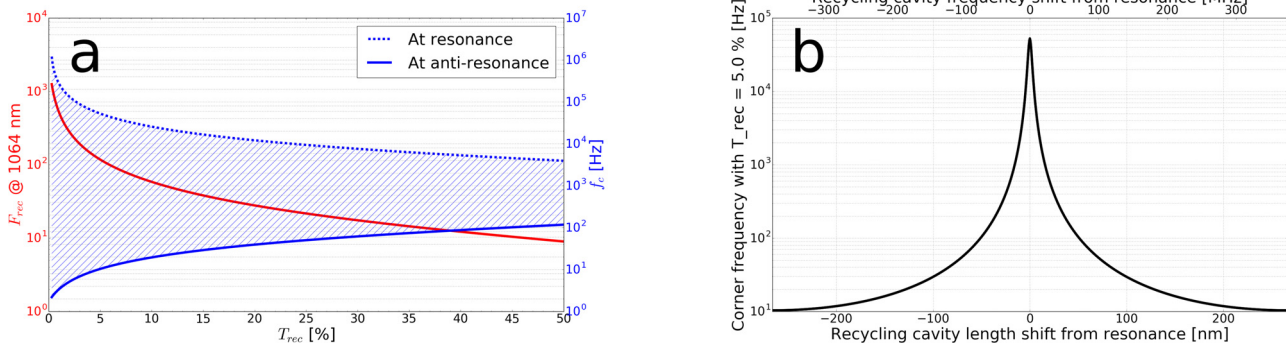


FIG. 20. Tuning the effective bandwidth of a cavity with a three-mirror cavity. (a) Cavity finesse \mathcal{F}_{rec} and corner frequency f_c as a function of the power transmission of the recycling cavity T_{rec} . The corner frequency is plotted in dashed line for the recycling cavity at resonance and in solid line for the recycling cavity at anti-resonance. The hatched area corresponds to accessible corner frequencies. (b) Corner frequency f_c for $T_{rec} = 5\%$ as a function of cavity shift from resonance.

crystal, pumped by a 532 nm laser beam, and placed inside an optical cavity, forming an optical parametric oscillator (OPO). After reflection on the filter cavity, the squeezed beam is measured on homodyne detection photodiodes by combination with a local oscillator (LO) beam at the exact same frequency. To ensure this condition, the 532 nm pump beam is generated by second harmonic generation (SHG) from the 1064 nm beam used for the local oscillator. A first analysis of the homodyne detection signal without squeezed beam is shown in Fig. 19. The local oscillator (LO) noise on the experiment done in-air has been measured to be shot-noise-limited between 1 and 3 kHz (cut-off frequency of the acquisition system) and 1 order of magnitude higher than the dark noise. This is where we expect to see noise reduction by the use of squeezing. Below 1 kHz, one can observe seismic noise and acoustic noise that should be reduced by placing the whole system under vacuum.

Parameters of the filter cavity can be tuned by adjusting its finesse through the addition of a recycling cavity on one end (see Fig. 18). The recycling mirror is placed 20 cm before the input mirror of the filter cavity. A simulation of the effect of the recycling cavity on the 50-m long test filter cavity is shown in Fig. 20. Depending on the resonance condition of the recycling cavity and the transmission of the recycling mirror T_{rec} , one can tune the corner frequency f_c of the filter cavity from a few Hz to 1 MHz with a finesse of the recycling cavity between 10 and 1000. For a given transmission of the recycling mirror, we can lock the recycling cavity at resonance for high corner frequency or anti-resonance for low corner frequency or even close to anti-resonance to slightly tune the corner frequency in between.

TABLE II. Summary of the status of our MQM experiments. The achievement of LKB1 is expressed by the remaining quanta n and the achievement of UT is expressed by the torque sensitivity.

	Oscillator	Effective mass	Resonance	Achievements
LKB1	Micropillar	$\sim 100 \mu\text{g}$	3.6 MHz	$n \sim 6$
LKB2	Membrane	$\sim 10 \text{ ng}$	5.7 MHz	$Q = 1.17 \times 10^6$
Gaku	Pendulum	7 mg	2.2 Hz	$Q = 2.0 \times 10^6$
UT	Torsion	10 mg	90 mHz	$20 \text{ aNm}/\sqrt{\text{Hz}}$
TT	Maglev	2 mg	16 Hz	$Q \sim 10^4$

XI. SUMMARY AND FUTURE PROSPECTS

Reaching the standard quantum limit is required to observe a quantum behavior of a macroscopic object and it is the key to test quantum mechanics. A possible standard of the boundary between the macroscopic and microscopic objects is the Planck mass. In this paper, we introduced a number of the state-of-the-art experiments using a test mass in various scale above the Planck mass. The suspension regime of those experiments can be categorized to three regimes: a mechanical resonator, a pendulum, and a levitation, and the preferable mass scale of each regime is a micro-gram scale, a gram scale, and an intermediate scale, respectively. The micropillar experiment at LKB has achieved to cool down the oscillator to a few remaining quanta, the micro-membrane experiment at LKB has achieved the Q factor of 1.17×10^6 , the monolithic pendulum experiment at Gakusyuhin has achieved the Q factor of 2.0×10^6 , the torsion pendulum experiment at UT has reached the torque sensitivity of $20 \text{ aNm}/\sqrt{\text{Hz}}$ around 100 Hz, the diamagnetic levitation experiment at Tokyo Tech has achieved the Q factor of $\sim 10^4$. Table II shows the summary of the experiments. Note that the Q factor can be higher with the use of the optomechanical spring and the expected gain is higher for the oscillator with a low resonant frequency. The optical levitation experiment at UT is not yet ready to measure the Q factor but has succeeded in showing the positive optical restoring force in the horizontal direction. In addition to the experiments to test the MQM, we introduced the quantum thermometry and the motion sensing with the squeeze light as the applications of the optomechanical effect. All the experiments have shown a good progress and are promising to test the MQM or to take the advantage of the technology in the near future.

ACKNOWLEDGMENTS

The authors acknowledge the support of the French Agence Nationale de la Recherche (ANR), under Grant Nos. ANR-14-CE26-0002 (project QuNat), ANR-15-CE30-0014 (project ExSqueeze), ANR-18-JSTQ-0002 (project QFilter), and ANR-21-CE47-0011 (project MecaFlux), and of the Japan Science and Technology Agency under JST CREST Grant No. JPMJCR1873. This research has also been funded by the Marie Curie Initial Training Network Cavity Quantum Optomechanics. S.C.

acknowledges support from the European Commission through Marie Curie Fellowship IIF Project SQZOMS No. 660941.

AUTHOR DECLARATIONS

Conflict of Interest

The authors have no conflicts to disclose.

Author Contributions

Michaël Croquette: Data curation (equal); Writing – original draft (equal). **Naoki Aritomi:** Data curation (equal). **Remy Braive:** Data curation (equal). **Tristan Briant:** Data curation (equal). **Stéphan Briaudeau:** Data curation (equal). **Seth B. Cataño-Lopez:** Data curation (equal). **Sheon Chua:** Data curation (equal). **Jérôme Degallaix:** Data curation (equal). **Masa-Katsu Fujimoto:** Data curation (equal). **Kyrylo Gerashchenko:** Data curation (equal). **François Glotin:** Data curation (equal). **Samuel Deléglise:** Data curation (equal); Writing – original draft (equal). **Pierre Gruning:** Data curation (equal). **Ken-ichi Harada:** Data curation (equal). **Antoine Heidmann:** Data curation (equal). **David Hofman:** Data curation (equal). **Pierre-Edouard Jacquet:** Data curation (equal). **Thibaut Jacqmin:** Data curation (equal). **Olga Kozlova:** Data curation (equal). **Nicolas Leroy:** Data curation (equal). **M. Vincent Loriette:** Data curation (equal). **Ferhat Loubar:** Data curation (equal). **Takuya Kawasaki:** Data curation (equal); Writing – original draft (equal). **Théo Martel:** Data curation (equal). **Rémi Metzdorff:** Data curation (equal). **Christophe Michel:** Data curation (equal). **Atsushi Mikami:** Data curation (equal). **Luis Najera:** Data curation (equal). **Leonhard Neuhaus:** Data curation (equal). **Sotasu Otabe:** Data curation (equal). **Laurent Pinard:** Data curation (equal). **Kaido Suzuki:** Data curation (equal). **Hiroki Takahashi:** Data curation (equal). **Kentaro Komori:** Data curation (equal); Writing – original draft (equal). **Kazuyuki Takeda:** Data curation (equal). **Yusuke Tominaga:** Data curation (equal). **Aymeric van de Walle:** Data curation (equal). **Naoki Yamamoto:** Data curation (equal). **Kentaro Somiya:** Data curation (equal); Writing – original draft (equal); Writing – review & editing (equal). **Pierre-François Cohadon:** Conceptualization (equal); Writing – original draft (equal); Writing – review & editing (equal). **Makoto Kuribayashi:** Data curation (equal); Writing – original draft (equal). **Angélique Lartaux-Vollard:** Data curation (equal); Writing – original draft (equal). **Nobuyuki Matsumoto:** Data curation (equal); Writing – original draft (equal). **Yuta Michimura:** Data curation (equal); Writing – original draft (equal). **Manuel Andia:** Data curation (equal); Writing – original draft (equal).

DATA AVAILABILITY

The data that support the findings of this study are available from the corresponding author upon reasonable request.

REFERENCES

- D. Ramos, E. Gil-Santos, V. Pini, J. M. Llorens, M. Fernández-Regúlez, A. San Paulo, M. Calleja, and J. Tamayo, *Nano Lett.* **12**, 932 (2012).
- M. Li, W. H. P. Pernice, and H. X. Tang, *Nat. Photonics* **3**, 464 (2009).
- P. F. Cohadon, A. Heidmann, and M. Pinard, *Phys. Rev. Lett.* **83**, 3174 (1999).
- O. Arcizet, P.-F. Cohadon, T. Briant, M. Pinard, and A. Heidmann, *Nature* **444**, 71 (2006).
- S. Gigan, H. R. Böhm, M. Paternostro, F. Blaser, G. Langer, J. B. Hertzberg, K. C. Schwab, D. Bäuerle, M. Aspelmeyer *et al.*, *Nature* **444**, 67 (2006).
- J. D. Teufel, T. Donner, D. Li, J. W. Harlow, M. S. Allman, K. Cicak, A. J. Sirois, J. D. Whittaker, K. W. Lehnert *et al.*, *Nature* **475**, 359 (2011).
- A. H. Safavi-Naeini, J. Chan, J. T. Hill, T. P. M. Alegre, A. Krause, and O. Painter, *Phys. Rev. Lett.* **108**, 033602 (2012).
- V. B. Braginsky, F. Y. Khalili, and K. S. Thorne, *Quantum Measurement* (Cambridge University Press, 1992).
- P. R. Saulson, *Phys. Rev. D* **42**, 2437 (1990).
- Y. Levin, *Phys. Rev. D* **57**, 659 (1998).
- F. Bondu, P. Hello, and J. Vinet, *Phys. Lett. A* **246**, 227 (1998).
- A. M. Gretarsson, G. M. Harry, P. R. Saulson, S. D. Penn, W. J. Startin, J. Hough, S. Rowan, and G. Cagnoli, *Phys. Lett. A* **270**, 108 (2000).
- D. J. Wilson, V. Sudhir, N. Piro, R. Schilling, A. Ghadimi, and T. J. Kippenberg, *Nature* **524**, 325 (2015).
- M. Rossi, D. Mason, J. Chen, Y. Tsaturyan, and A. Schliesser, *Nature* **563**, 53 (2018).
- A. G. Kuhn, M. Bahriz, O. Ducloux, C. Chartier, O. Le Traon, T. Briant, P.-F. Cohadon, A. Heidmann, C. Michel *et al.*, *Appl. Phys. Lett.* **99**, 121103 (2011).
- M. Poggio, C. L. Degen, H. J. Mamin, and D. Rugar, *Phys. Rev. Lett.* **99**, 017201 (2007).
- D. Hälgl, T. Gislser, Y. Tsaturyan, L. Catalini, U. Grob, M.-D. Krass, M. Héritier, H. Mattiat, A.-K. Thamm *et al.*, *Phys. Rev. Appl.* **15**, L021001 (2021).
- R. W. Andrews, R. W. Peterson, T. P. Purdy, K. Cicak, R. W. Simmonds, C. A. Regal, and K. W. Lehnert, *Nat. Phys.* **10**, 321 (2014).
- M. F. Gely and G. A. Steele, *AVS Quantum Sci.* **3**, 035601 (2021).
- Y. Tsaturyan, A. Barg, E. S. Polzik, and A. Schliesser, *Nat. Nanotechnol.* **12**, 776 (2017).
- A. H. Ghadimi, S. A. Fedorov, N. J. Engelsens, M. J. Beryehi, R. Schilling, D. J. Wilson, and T. J. Kippenberg, *Science* **360**, 764 (2018).
- Q. P. Unterreithmeier, T. Faust, and J. P. Kotthaus, *Phys. Rev. Lett.* **105**, 027205 (2010).
- P.-L. Yu, T. P. Purdy, and C. A. Regal, *Phys. Rev. Lett.* **108**, 083603 (2012).
- E. Ivanov, T. Capelle, M. Rosticher, J. Palomo, T. Briant, P.-F. Cohadon, A. Heidmann, T. Jacqmin, and S. Deléglise, *Appl. Phys. Lett.* **117**, 254102 (2020).
- L. G. Villanueva and S. Schmid, *Phys. Rev. Lett.* **113**, L27201 (2014).
- A. M. Jayich, J. C. Sankey, B. M. Zwickl, C. Yang, J. D. Thompson, S. M. Girvin, A. A. Clerk, F. Marquardt, and J. G. E. Harris, *New J. Phys.* **10**, 095008 (2008).
- R. A. Norte, J. P. Moura, and S. Gröblacher, *Phys. Rev. Lett.* **116**, 147202 (2016).
- X. Chen, C. Chardin, K. Makles, C. Caër, S. Chua, R. Braive, I. Robert-Philip, T. Briant, P.-F. Cohadon *et al.*, *Light Sci. Appl.* **6**, e16190 (2017).
- J. Guo, R. A. Norte, and S. Gröblacher, *Opt. Express* **25**, 9196 (2017).
- M. Yuan, M. A. Cohen, and G. A. Steele, *Appl. Phys. Lett.* **107**, 263501 (2015).
- Y. Seis, T. Capelle, E. Langman, S. Saarinen, E. Planz, and A. Schliesser, *Nat. Commun.* **13**, 1507 (2022).
- J. Viennot, X. Ma, and K. W. Lehnert, *Phys. Rev. Lett.* **121**, 183601 (2018).
- L. Najera *et al.*, “Sideband cooling of a radio-frequency qubit” (unpublished).
- S. B. Cataño Lopez, J. G. Santiago-Condori, K. Edamatsu, and N. Matsumoto, *Phys. Rev. Lett.* **124**, 221102 (2020).
- S. D. Penn, A. Ageev, D. Busby, G. M. Harry, A. M. Gretarsson, K. Numata, and P. Willems, *Phys. Lett. A* **352**, 3 (2006).
- C. J. Bell, S. Reid, J. Faller, G. D. Hammond, J. Hough, I. W. Martin, S. Rowan, and K. V. Tokmakov, *Classical Quantum Gravity* **31**, 065010 (2014).
- N. Matsumoto, S. B. Cataño Lopez, M. Sugawara, S. Suzuki, N. Abe, K. Komori, Y. Michimura, Y. Aso, and K. Edamatsu, *Phys. Rev. Lett.* **122**, 071101 (2019).
- J. A. Sidles and D. Sigg, *Phys. Lett. A* **354**, 167 (2006).
- D. Sigg, see www.ligo.caltech.edu/docs/T/T030275-00.pdf for a discussion of the angular instability in a triangular cavity (2003).
- N. Matsumoto, Y. Michimura, Y. Aso, and K. Tsubono, *Opt. Express* **22**, 12915 (2014).
- D. Miki, N. Matsumoto, A. Matsumura, T. Shichijo, Y. Sugiyama, K. Yamamoto, and N. Yamamoto, “Generating quantum entanglement between macroscopic objects with continuous measurement and feedback control,” *arXiv:2210.13169* (2022).
- H. Cavendish, “Experiments to determine the density of the earth,” *Philos. Trans. R. Soc.* **88**, 469 (1798).

- ⁴³T. A. Wagner, S. Schlamminger, J. H. Gundlach, and E. G. Adelberger, *Classical Quantum Gravity* **29**, 184002 (2012).
- ⁴⁴E. Adelberger, B. Heckel, and A. Nelson, *Annu. Rev. Nucl. Part. Sci.* **53**, 77 (2003).
- ⁴⁵B. A. Stickler, B. Papendell, S. Kuhn, B. Schriniski, J. Millen, M. Arndt, and K. Hornberger, *New J. Phys.* **20**, 122001 (2018).
- ⁴⁶G. C. Ghirardi, A. Rimini, and T. Weber, *Phys. Rev.* **34**, 470 (1986).
- ⁴⁷R. Penrose, *Gen. Relativ. Gravitation* **28**, 581 (1996).
- ⁴⁸W. Marshall, C. Simon, R. Penrose, and D. Bouwmeester, *Phys. Rev. Lett.* **91**, 130401 (2003).
- ⁴⁹L. Diósi, *Phys. Rev. Lett.* **114**, 050403 (2015).
- ⁵⁰A. Bassi, A. Großardt, and H. Ulbricht, *Classical Quantum Gravity* **34**, 193002 (2017).
- ⁵¹I. Pikovski, M. R. Vanner, M. Aspelmeyer, M. S. Kim, and Č. Brukner, *Nat. Phys.* **8**, 393 (2012).
- ⁵²D. Kafri, G. J. Milburn, and J. M. Taylor, *New J. Phys.* **17**, 015006 (2015).
- ⁵³J. Schmöle, M. Dragosits, H. Hepach, and M. Aspelmeyer, *Classical Quantum Gravity* **33**, 125031 (2016).
- ⁵⁴B. Helou, J. Luo, H.-C. Yeh, C.-g. Shao, B. J. J. Slagmolen, D. E. McClelland, and Y. Chen, *Phys. Rev. D* **96**, 044408 (2017).
- ⁵⁵A. A. Balushi, W. Cong, and R. B. Mann, *Phys. Rev. A* **98**, 043811 (2018).
- ⁵⁶Y. Michimura and K. Komori, *Eur. Phys. J. D* **74**, 126 (2020).
- ⁵⁷K. Komori, Y. Enomoto, C. P. Ooi, Y. Miyazaki, N. Matsumoto, V. Sudhir, Y. Michimura, and M. Ando, *Phys. Rev. A* **101**, 011802 (2020).
- ⁵⁸A. R. Neben, T. P. Bodiya, C. Wipf, E. Oelker, T. Corbitt, and N. Mavalvala, *New J. Phys.* **14**, 115008 (2012).
- ⁵⁹N. Matsumoto, K. Komori, Y. Michimura, G. Hayase, Y. Aso, and K. Tsubono, *Phys. Rev. A* **92**, 033825 (2015).
- ⁶⁰T. T.-H. Nguyen, C. M. Mow-Lowry, B. J. J. Slagmolen, J. Miller, A. J. Mullavey, S. Goßler, P. A. Altin, D. A. Shaddock, and D. E. McClelland, *Phys. Rev. D* **92**, 112004 (2015).
- ⁶¹T. Kawasaki, K. Komori, H. Fujimoto, Y. Michimura, and M. Ando, *Phys. Rev. A* **106**, 013514 (2022).
- ⁶²F. Tebbenjohanns, M. Frimmer, V. Jain, D. Windey, and L. Novotny, *Phys. Rev. Lett.* **124**, 013603 (2020).
- ⁶³U. Delić, M. Reisenbauer, K. Dare, D. Grass, V. Vuletić, N. Kiesel, and M. Aspelmeyer, *Science* **367**, 892 (2020).
- ⁶⁴P. R. Magrini, C. Bach, A. Deutschmann-Olek, S. G. Hofer, S. Hong, N. Kiesel, A. Kugi, and M. Aspelmeyer, *Nature* **595**, 373 (2021).
- ⁶⁵G. Guccione, M. Hosseini, S. Adlong, M. T. Johnsson, J. Hope, B. C. Buchler, and P. K. Lam, *Phys. Rev. Lett.* **111**, 183001 (2013).
- ⁶⁶Y. Michimura, Y. Kuwahara, T. Ushiba, N. Matsumoto, and M. Ando, *Opt. Express* **25**, 13799 (2017).
- ⁶⁷C. T. M. Ho, R. B. Mann, and T. C. Ralph, “Quantum optical levitation of a mirror,” [arXiv:1911.02705](https://arxiv.org/abs/1911.02705) (2019).
- ⁶⁸T. Kawasaki, N. Kita, K. Nagano, S. Wada, Y. Kuwahara, M. Ando, and Y. Michimura, *Phys. Rev. A* **102**, 053520 (2020).
- ⁶⁹G. Janssen, M. Abdalla, F. van Keulen, B. Pujada, and B. van Venrooy, *Thin Solid Films* **517**, 1858 (2009).
- ⁷⁰B. V. Jayawant, *Rep. Prog. Phys.* **44**, 411 (1981).
- ⁷¹R. W. P. Drever, “Techniques for extending interferometer performance using magnetic levitation and other methods,” in *Proceedings of the International Conference on Gravitational Waves (Source and Detectors)*, edited by I. Ciufolini, F. Fidicaro (World Scientific, 1996).
- ⁷²A. Giazotto, *Phys. Lett. A* **245**, 203 (1998).
- ⁷³R. Nakashima, *Phys. Lett. A* **384**, 126592 (2020).
- ⁷⁴B. Fellmuth, J. Fischer, G. Machin, S. Picard, P. P. M. Steur, O. Tamura, D. R. White, and H. Yoon, *Philos. Trans. R. Soc. A* **374**, 20150037 (2016).
- ⁷⁵N. Klimov, T. Purdy, and Z. Ahmed, *Sens. Actuators, A* **269**, 308 (2018).
- ⁷⁶T. P. Purdy, K. E. Grutter, K. Srinivasan, and J. M. Taylor, *Science* **356**, 1265 (2017).
- ⁷⁷J. F. Qu, S. P. Benz, H. Rogalla, W. L. Tew, D. R. White, and K. L. Zhou, *Meas. Sci. Technol.* **30**, 112001 (2019).
- ⁷⁸C. M. Caves, *Phys. Rev. Lett.* **45**, 75 (1980).
- ⁷⁹F. Acernese *et al.*, *Phys. Rev. Lett.* **123**, 231108 (2019).
- ⁸⁰H. J. Kimble, Y. Levin, A. B. Matsko, K. S. Thorne, and S. P. Vyatchanin, *Phys. Rev. D* **65**, 022002 (2001).
- ⁸¹A. Lartaux-Vollard, “Beating the standard quantum limit for the gravitational wave detector advanced Virgo,” Ph.D. thesis (Université Paris-Saclay, 2020).